Journal of Earth Science, Vol. 24, No. 1, p. 125–135, February 2013 *ISSN 1674-487X*
Printed in China
DOI: 10.1007/s12583-013-0316-3

Automated Rock Detection and Shape Analysis from Mars Rover Imagery and 3D Point Cloud Data

Kaichang Di* (邸凯昌), **Zongyu Yue** (岳宗玉), **Zhaoqin Liu** (刘召芹)
State Key Laboratory of Remote Sensing Science, Institute of Remote Sensing Applications, Chinese Academy Sciences, Beijing 100101, *China*
Shuliang Wang (王树良)
School of Software, Beijing Institute of Technology, Beijing 100081, *China*

ABSTRACT: A new object-oriented method has been developed for the extraction of Mars rocks from Mars rover data. It is based on a combination of Mars rover imagery and 3D point cloud data. First, Navcam or Pancam images taken by the Mars rovers are segmented into homogeneous objects with a mean-shift algorithm. Then, the objects in the segmented images are classified into small rock candidates, rock shadows, and large objects. Rock shadows and large objects are considered as the regions within which large rocks may exist. In these regions, large rock candidates are extracted through ground-plane fitting with the 3D point cloud data. Small and large rock candidates are combined and postprocessed to obtain the final rock extraction results. The shape properties of the rocks (angularity, circularity, width, height, and width-height ratio) have been calculated for subsequent geological studies.

KEY WORDS: Mars rover, rock extraction, rover image, 3D point cloud data.

INTRODUCTION

Rocks are one of the major features exposed on the Martian surface. For Mars rover missions, they can play an important role both in scientific research and engineering operations. Firstly, rocks can provide considerable rich information for the study of planetary geology. For example, rocks can provide clues for physical parameters, such as the temperature and pressure needed to create certain rocks, which is critical for understanding of the planet's chemical composition and geologic environment (Gor et al., 2001). Rocks can also tell us what has happened after their formation, indirectly suggesting, through changes to their shape properties, corresponding planetary geologic processes such as the effect of climate, erosion, and transposition mechanics. Secondly, rocks can be used to evaluate the information content of an image and, thereby, assist in images compression and prioritization of data transmission from Mars to the Earth. This is especially meaningful today when instruments are capable of collecting much more data than it is practicable to return to the Earth (Anderson et al., 2001; Gor et al., 2001; Manduchi et al., 2000). In future Mars rover missions, the rovers will travel much longer distances than those have achieved by the Mars Exploration Rover (MER) 2003 Spirit and Opportunity rovers, and many images of the Martian

This study was supported by the National Natural Science Foundation of China (Nos. 41171355 and 41002120).

*Corresponding author: kcdi@irsa.ac.cn

Manuscript received June 19, 2012.
Manuscript accepted October 11, 2012.

surface collected by the rovers might have no chance to be studied by scientists. Therefore, onboard autonomous image analysis is highly desirable in future Mars rover exploration missions (Thompson et al., 2005a; Wagstaff et al., 2004). Autonomous rock detection and analysis will be one of the major parts of such an autonomous image analysis system for Mars exploration. Thirdly, rocks are one of the major obstacles for rover traversing, with the capacity to endanger rover safety if not detected correctly in advance. Fourthly, rocks are ideal for use as tie points for vision-based rover localization and navigation (Li et al., 2007). Therefore, autonomous rock detection is valuable both for planetary geology study and for hazard avoidance and rover localization in Mars mission operations.

In general, identifying rocks in intensity images of a planetary surface is very challenging, especially because no uniform morphology, color, texture, or other measures exist to characterize rocks from other features. In addition, rocks often are covered by dust and/or can occlude (hide) each other, becoming blurred in the distance or becoming partially embedded in the terrain (Thompson and Castano, 2007). For rock extraction, good sources of complementary information about image intensity can be 3D point cloud data or range data.

A number of methods for rock detection from rover imagery have been developed for different purposes. Castano et al. (2005) developed an edge-based rock-detection algorithm that runs at multiple levels of an image pyramid in order to detect rocks (closed-edge shapes) of all sizes. Gor et al. (2001) developed a rock detection method in which small rocks are detected using image intensity information through edge-flow segmentation, while large rocks are detected using range information (derived from stereo intensity images) through ground-plane fitting and height segmentation. Small and large rocks are detected by separately evaluating the intensity values and range data in an image and then merging together the results to determine the final rock identifications. In the merge process, if intensity-based and range-based detections overlap, range-based detections always take precedence. These rock-detection algorithms have been included in the NASA Jet Propulsion Laboratory's Onboard Autonomous Science Investigation System and tested for autonomous rock shape analysis, being used to direct the rover to regions of higher geologic significance (Castano et al., 2007, 2005). Gulick et al. (2001) developed a rock detector based on cast shadows, applying the algorithm to help select targets for infrared spectral analysis in the 1999 Marsokhod rover field test in Silver Lake, California. Thompson et al. (2005b) developed a rock-detection method based on segmentation, detection, and classification using texture, color, shape, shading, and stereo data. Song and Shan (2008, 2006) developed a framework for automated rock segmentation from Mars rover imagery through texture-based image segmentation and rock-boundary refinement using an edge-flow-driven active contour model. Thompson and Castano (2007) evaluated the performances of seven rock-detection algorithms with respect to several autonomous geologic applications, such as target selection (finding pixels that are most likely to lie on the surface of a rock) and autonomous site characterization. It was found that rock-detection algorithms perform well for target selection, but absolute quantitative site descriptions appear beyond the capability of current detectors (Thompson and Castano, 2007). Li et al. (2007) developed a method to extract large rocks from three-dimensional ground points generated from stereo images to enable automation of cross-site tie-point selection for bundle-adjustment-based rover localization.

In this research, we have developed a new rock-detection algorithm based on object-oriented combination of image intensity and 3D point cloud data. It includes a series of steps: image segmentation, small and large object categorization, separation of small rocks and shadow objects, large rock detection through plane-fitting of 3D point-cloud data, and final rock extraction from the combination of small and large rock candidates with post-processing.

The shape of a rock, which is useful for geological analysis, is a complex property that is often difficult to describe precisely. Many parameters (indices) have been developed for depicting shape properties, and generally, there are good correlations among these indices (Fox et al., 2002). In this research, five parameters have been used to describe the shape of a

rock: angularity, circularity, width, height, and width-height ratio (width/height). The first two parameters are derived through least-squares ellipse fitting of the rock boundary; they give quantitative measurements for the evaluation of the degree of erosion, which is something that is helpful for inferring how far the rock has traveled and its antierosion ability (Castano et al., 2002). The remaining three parameters, computed from direct measurements, represent fundamental data for size-frequency analysis, which can be used to infer the geological history of a region (Golombek et al., 2008).

MARS ROVER IMAGES AND 3D POINT CLOUD DATA

In this rock extraction study, images acquired by the NASA Mars Exploration Rover (MER) 2003 rover Spirit were used along with the derived 3D point cloud data. Among the imaging sensors carried by the MER rovers, navigation cameras (Navcam), which are a pair of monochrome stereo cameras mounted on the camera bar of the rover, have been constantly used during mission operations for navigation and terrain mapping (Alexander et al., 2006; Li et al., 2005). Panoramic cameras (Pancam), which are a pair of multispectral stereo cameras mounted on the same camera bar, have been used for scientific investigation of the morphology, topography, and geology, etc., of the landing site. The epipolar-resampled Navcam and Pancam images, which were automatically generated by the Multimission Image Processing Laboratory (MIPL) of the Jet Propulsion Laboratory (JPL) with its software pipeline, are directly downloaded from the MER Analyst's Notebook website (http://anserver1.eprsl.wustl.edu/). These images are published in .pds format and defined as FFL files. Figure 1 shows the left image of a stereo pair taken at Site 96 by the Spirit rover Navcam. Rocks having different sizes can be identified clearly by human sight.

Three-dimensional point cloud data are derived

Figure 1. Left image of a Navcam stereo pair taken by the Spirit rover at Site 96 (Image ID: 2N155309000FFL9600P0655L0M1.img).

from stereo images and are defined as XYL files in the MER Analyst's Notebook. The data are stored with the index of the epipolar-resampled (FFL) left image of stereo pairs, and the pixel values are ground coordinates *X*, *Y*, and *Z* in the local site coordinate system (Di et al., 2008) where *Z* represents down. The data were also published in .pds format and the metadata of the image is stored in the file header. Figure 2 shows the image of the *Z* values in the 3D point cloud data derived from the stereo images shown in Figure 1. The pixels between the two images are of one-to-one correspondence. In the *Z* image, the grayer the pixels, the higher the elevation except that the dark pixels represent null values, i.e., where there is no 3D information available on these pixels. These dark pixels are basically pixels that have no reliable stereo image matching results. They include the following: 1) upper parts of the image that are too far from the camera; 2) left, right, and lower boundary areas that have no overlap with the right image; 3) pixels that have no texture in local areas; and 4) pixels that have sudden parallax change such as the pixels next to the up boundaries of large rocks. It is easy to understand that image matching quality affects the quality of the derived 3D point cloud data and consequently affects rock extraction results.

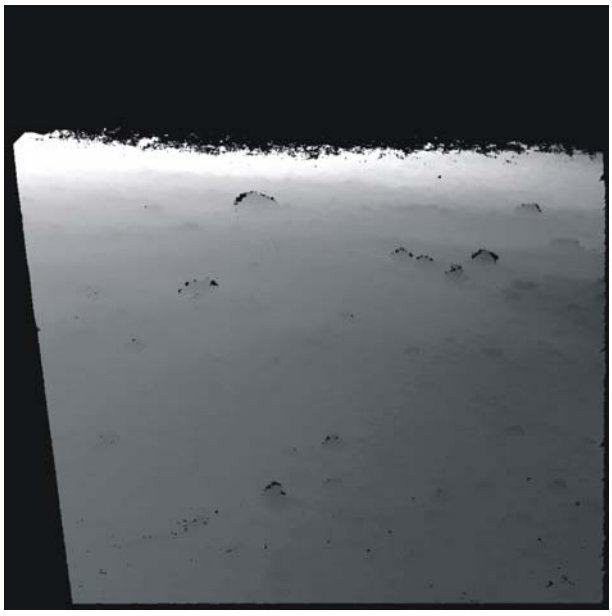

Figure 2. Image of the *Z* values in the 3D point cloud data corresponding to Fig. 1.

AUTOMATED ROCK EXTRACTION AND SHAPE ANALYSIS

Figure 3 shows the flowchart of the proposed method of rock extraction and shape analysis. The Mars rover intensity image is first segmented by a mean-shift algorithm. Then, small rock candidates, shadow objects, and large objects are detected. Next, ground-plane fitting is performed in regions around the large objects and around shadow objects; large rock candidates are extracted from the pixels above the fitted ground planes. Consequently, rocks are identified from the combination of small and large rock candidates with a post-processing process. Finally, shape parameters angularity and circularity are computed from ellipse fitting of rock boundaries; width, height, and width-height ratio are computed from size measurements. The details of the algorithms are described below. It is worth to note that we also tried other segmentation methods (including edge-flow) in the first step, and the mean-shift method generally performs better in our experiments with the MER data.

Mean-Shift Segmentation of Rover Image and Small Rock Extraction

The concept of mean shift was first presented by Fukunaga and Hostetler in 1975 (Fukunaga and Hostetler, 1975) and was popularized by Cheng (1995) and Comaniciu et al. (Comaniciu and Meer, 2002; Comaniciu et al., 2001, 2000) in the field of image processing. In recent years, much study has been devoted to analysis of such of its properties as bandwidth selection (Comaniciu et al., 2001), kernel function (Peng et al., 2005), and convergence (Wen and Cai, 2007). Mean shift is essentially a method of nonparametric statistics, which is a mode-seeking process through a simple iterative procedure that shifts each data point to the average of data points in its neighborhood with a kernel function. Mean shift has been extensively used in applications, such as clustering (Ozertem et al., 2008; Wu and Yang, 2007), segmentation (Hong et al., 2007), target tracking (Comaniciu et al., 2000), and discontinuity preserving smoothing (Comaniciu and Meer, 2002). The process of mean-shift segmentation of a MER rover image is listed as follows.

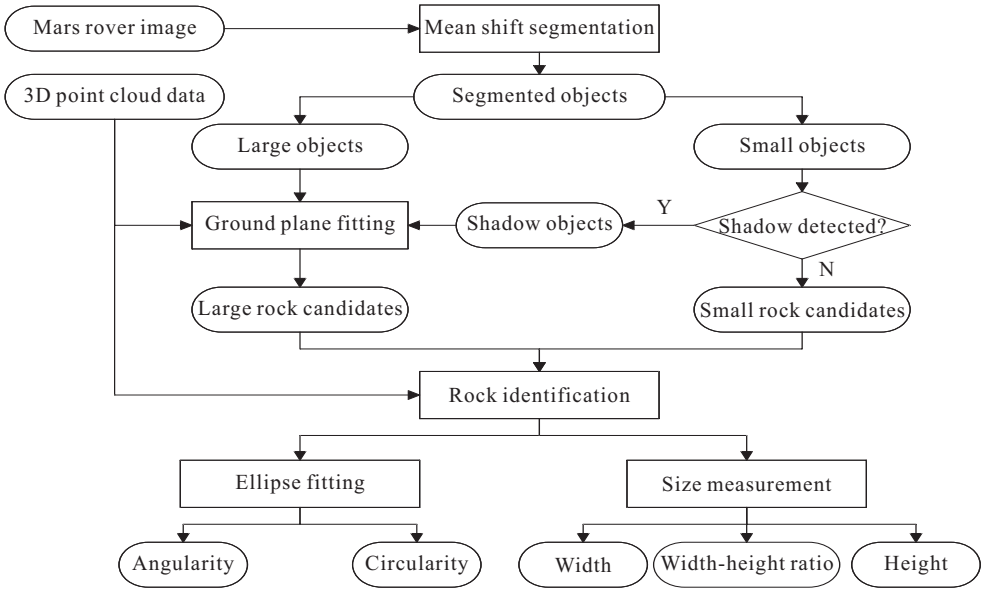

Figure 3. Flowchart of the proposed method of rock extraction and shape analysis.

(1) Transform the rover image to 3D vectors including spatial and range domains. Spatial domain refers to the lattice (row and column) of the image, and range domain refers to the grayscale values. Both domains are normalized.

(2) Calculate the sequence of successive center locations of the vectors with selected kernel function. Run the procedure for all the image vectors and store the information for all convergence points.

(3) Group together all convergence points that can satisfy both the thresholds in the spatial and range domains and concatenate the corresponding convergence points.

(4) Consider each convergence basin is as an object and eliminate those regions with areas less than a threshold.

In this research, the image segmentation is realized using a public code named EDISON (Edge Detection and Image Segmentation) developed by Comaniciu (Comaniciu, 2009). In this program, the following parameters should be predefined: spatial size (windows), range threshold (grayscale value), and number of pixels in the minimum region. The general rule for parameter selection is that a large spatial size is suitable for big objects and higher range threshold for stronger image contrast. The parameter for the number of pixels of the minimum region depends on the minimum object to be extracted. In our study, many comparative experiments were performed to get empirical values of the parameters. As a result, the default parameters of 7 and 6.5 were set for spatial size and intensity, respectively, and minimum region was set to 50 pixels for all the tested MER images. The sequence of successive locations and the selected kernel function can be denoted as

$$y_{j+1} = \frac{\sum_{i=1}^{n} x_i g\left(\left\|\frac{x - x_i}{h}\right\|^2\right)}{\sum_{i=1}^{n} g\left(\left\|\frac{x - x_i}{h}\right\|^2\right)}, j = 1,2,\ldots \quad (1)$$

where h is the bandwidth parameter. A flat kernel function was used

$$g(x) = \begin{cases} 1, \|x\| \le 1 \\ 0, \|x\| > 1 \end{cases} \quad (2)$$

in which the x is the vector including spatial size and range domain.

After mean-shift segmentation, the single object with the most number of pixels is identified as the background and is eliminated. The remaining objects are divided into small objects and large objects according their areas. Objects with areas less than a threshold (e.g., 800 pixels) are classified as small objects. The threshold is an empirical value, and the result is not very sensitive to it.

Figure 4a shows the results of mean-shift segmentation of the image in Figure 1 after the removal of the background. The solid lines show the boundaries of small objects, and the dashed lines show the

boundaries of large objects. It can be seen that most of the small rocks are exactly delineated. However, many relatively large rocks cannot be delineated well because of varying lighting conditions on different sides of the rock or because of significant changes in intensity and/or texture on different parts of the rock. As a result, large rocks are often only partially extracted. Figures 4b and 4c are enlarged portions of the two examples marked by arrows in Fig. 4a. The large rock in Fig. 4b is only partially segmented, being detected as a large object; the shadow area of the large rock in Fig. 4c is segmented and detected as a small object. By experimenting with tens of images, it was found that the mean-shift segmentation can extract most of the small rocks correctly but often only partially extracts large rocks. It was also observed that many dark small areas are self and/or cast shadows, which thus provide clues for the existence of large rocks. To distinguish these dark small objects (shadows) from regular small objects, a simple method was used based on the setting of two thresholds: one for the mean (e.g., 40) and the other for the standard deviation (e.g., 15) of the object. If the mean and standard deviation of a small object are less than the predefined thresholds, it is considered to be a shadow. Small objects that are not considered as shadows are then identified as small rock candidates. Shadow objects and large objects are further processed by using 3D point cloud data to more precisely extract large rocks.

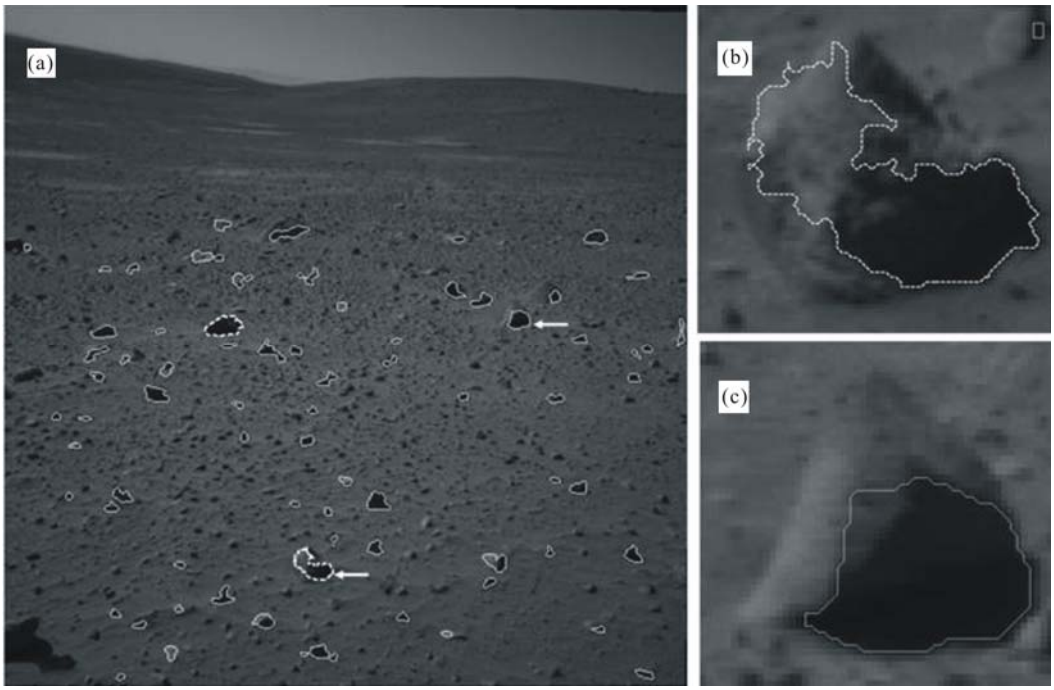

Figure 4. Objects extracted from mean-shift segmentation of Fig. 1 and enlarged portions (4b and 4c) corresponding to the arrows in Fig. 4a.

Extraction of Large Rocks from 3D Point Cloud Data Based on Targeted Ground-Plane Fitting

Three-dimensional point data provides the elevation information for each pixel of a rover image. This data can be used as complementary information, especially for the extraction of large rocks. Gor et al. used range data to calculate the height for every pixel by fitting a least-squares plane to the range data (Gor et al., 2001). In this research, ground-plane fitting is only performed at targeted regions where large rocks are most likely to exist, e.g., regions with large objects or shadow objects from the previous image-segmentation step. This will make the plane-fitting and large-rock-extraction processes more efficient, and potentially, more reliable than would fitting a ground plane at every pixel. Minimum bounding rectangles (MBRs) of the boundaries of the large objects and the shadow objects are generated; they are expanded all round in such a way that the width and height of the expanded region are twice the width and height of the original

MBRs. In this way, the fitting regions (expanded rectangular regions) are large enough to surround the entire rock. The mathematical equation for plane fitting is

$$Z = AX + BY + C \quad (3)$$

where A, B, and C are the parameters to be solved for through the least-squares fitting process. The perpendicular distance from a 3D point (X_0, Y_0, Z_0) to the fitted plane is calculated as

$$d = \left| \frac{AX_0 + BY_0 + C - Z_0}{\sqrt{A^2 + B^2 + 1}} \right| \quad (4)$$

Fitting of a ground plane is done iteratively. In each iteration, only the 3D points under the fitted plane instead of the points within three standard deviations from mean (as used in Gor et al., 2001) are used to refit the plane. Usually, refitting the plane three times produces good results. In the end, if a pixel is 0.02 m higher than the resultant fitted ground plane, it is detected as large rock pixel. Connected large rock pixels are grouped, and the boundary of the large rock is then delineated.

Final Rock Extraction

The small and large rock candidates extracted from the above steps are combined and post-processed for final rock extraction. Because rocks too far from the camera are not reliably detected due to the limit of stereo ranging capability, rock candidates beyond 30 m from the camera are eliminated. Meanwhile, since very small rocks are not significant for scientific study, rock candidates whose maximum height differences within the rock are less than 0.05 m are also eliminated. After this post-processing with constraints of maximum distance to the camera and maximum elevation difference within the rock candidates, the remaining rock candidates are taken as final rocks.

Analysis of Rock Shape

The shape parameters angularity and circularity of a rock are derived from modeling the rock by an ellipse in image space with a least-squares fitting method. To fit the rock by an ellipse rather than by general conics, some constraint conditions among the parameters of the conic must be imposed. Here, a robust ellipse fitting method developed by Fitzgibbon et al. (1999) was adopted. In this method, the ellipse is represented by a general conic

$$F(x, y) = ax^2 + bxy + cy^2 + dx + ey + f = 0 \quad (5)$$

with the following constraint

$$b^2 - 4ac = -1 \quad (6)$$

An ellipse fitting error is represented by the root mean residual error

$$s = \sqrt{\frac{\sum_{i=1}^{n} F^2(x_i, y_i)}{n}} \quad (7)$$

As mentioned in Fox et al. (2002), the ellipse fitting error concurs with an angularity measure. Here, we use this ellipse fitting error as an angularity error. Its value ranges from 0 to positive infinity; the higher the angularity value, the more angular is the rock.

The other shape parameter is circularity or the eccentricity of the ellipse. If we represent the semimajor and semiminor axes of the ellipse by a and b and suppose that $a^2 = b^2 + c^2$, then

$$e = \frac{c}{a} \quad (8)$$

This value ranges from 0 to 1; the smaller the value, the more circular is the rock.

EXPERIMENTAL RESULTS

Tens of Navcam and Pancam images taken by the MER Spirit rover (downloaded from the MER Analyst's Notebook) were processed using this method. In general, satisfactory results were obtained.

Figure 5 shows representative results. Figure 5a shows the result of rock extraction of the Navcam images, as shown in Fig. 1. Figures 5b and 5c show the results of two other Navcam images (2N155489638FFL9700 P0655L0M1.img and 2N155309050FFL9600P0655 L0M1.img). For comparison purposes, Fig. 6d shows the result of rock extraction of a Pancam image (blue channel, 2P192063629FFLANO8P2359L7 M1.img). As can be seen, most rocks significant to scientific study have been successfully extracted, indicating that the overall performance of the developed rock extraction method is satisfactory. In some areas, where rocks are occluded or stuck together, two rocks are extracted as one rock. In areas with large slopes (such as in Fig. 5d), a number of rocks are partially extracted. These cases should be further investigated for the

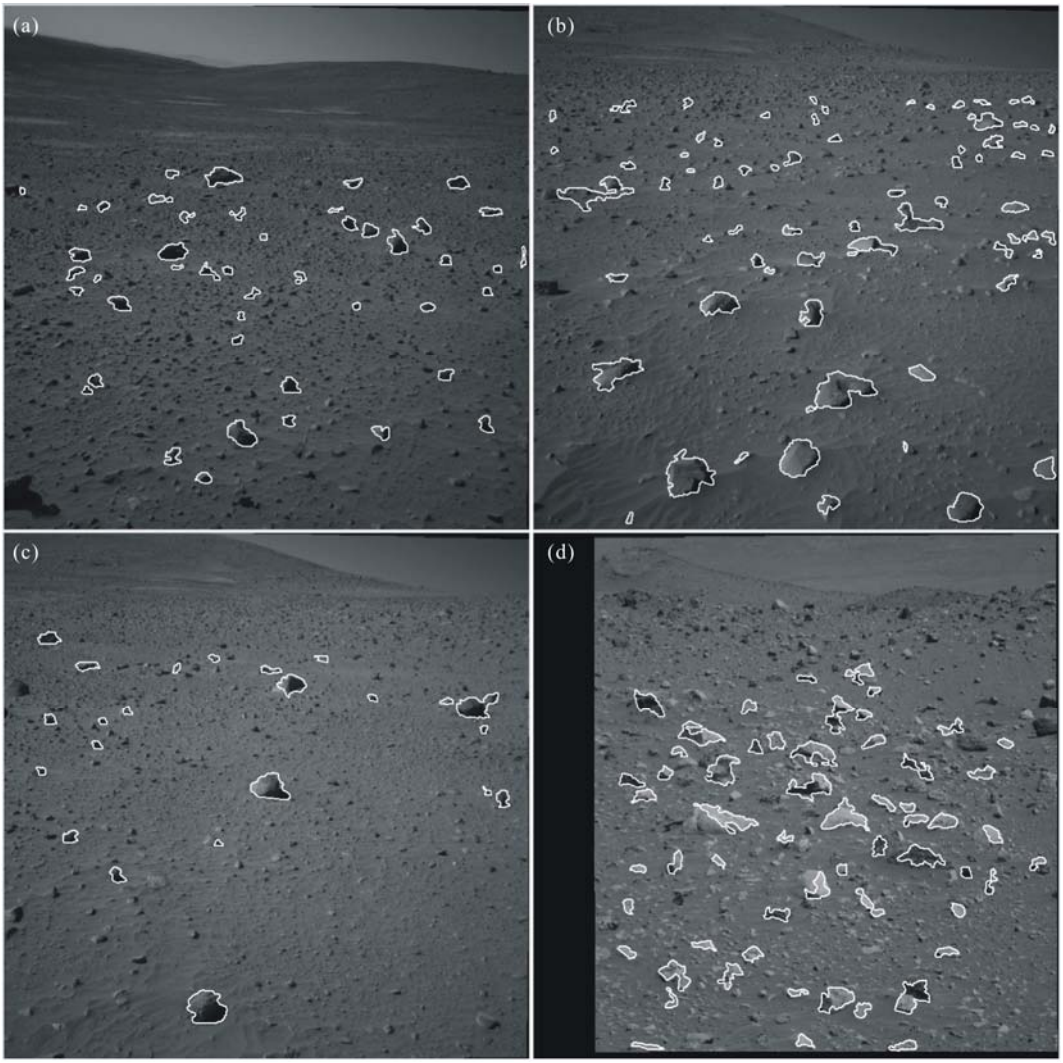

Figure 5. Results of rock extraction from Navcam and Pancam images taken by the Spirit rover.

improvement of this rock extraction method.

Figure 6 shows typical examples of the extracted rocks and fitted ellipses from the above images. The directions of principle axes of the fitted ellipses are also shown in the figure. Table 1 lists the statistics of angularity, circularity, width, height, and width/height of these rocks. The ID numbers of the rocks correspond to the numbers noted in Fig. 6. These parameters can generally give the shape information for extracted rocks. For example, Rock 11 has the maximum angularity; it is obviously more irregular than others. The circularity of Rock 14 is the minimum, which is consistent with its more circular appearance. With the extracted rocks and their shape parameters, it is easy to perform intelligent queries, such as finding the most circular rock, the most irregular rock, and the largest rock, etc.. This kind of query is very useful for geological analysis and science target designation.

CONCLUSIONS

A new rock detection method has been developed based on an object-oriented combination of image intensity and 3D point cloud data. Experiment results using NASA MER Spirit rover data demonstrate the effectiveness of the method. Overall, segmentation of image intensity usually can extract small rocks well, while plane fitting of 3D point cloud data provides more complete information about large rocks. An object-oriented combination of image intensity and 3D point cloud data can extract most of the rocks in Mars rover images. The extracted rocks and derived shape parameters are valuable for geological study as well as

Table 1 Shape parameters of the rocks in Fig. 6

ID No.	Angularity	Circularity	Width (cm)	Height (cm)	Width/height	Image
1	0.392 74	0.812 06	0.341 58	1.153	0.296 25	2N155309000FFL9600P0655L0M1.img
2	0.173 50	0.739 45	0.078 7	0.071 9	1.094 58	2N155309000FFL9600P0655L0M1.img
3	0.907 77	0.709 25	0.099 11	0.108 87	0.910 35	2N155309050FFL9600P0655L0M1.img
4	0.407 99	0.713 29	0.343 75	0.608 84	0.564 60	2N155309050FFL9600P0655L0M1.img
5	0.420 93	0.674 95	0.090 88	0.174 27	0.521 49	2N155309050FFL9600P0655L0M1.img
6	0.367 39	0.686 16	0.113 25	0.145 26	0.779 64	2N155391904FFL9600P1755L0M1.img
7	0.552 91	0.907 47	0.259 26	0.371 02	0.698 78	2N155489602FFL9700P0655L0M1.img
8	0.173 90	0.686 84	0.107 9	0.145 19	0.743 16	2N155489602FFL9700P0655L0M1.img
9	0.445 11	0.723 98	0.329 35	0.758 93	0.433 97	2N155489602FFL9700P0655L0M1.img
10	0.304 97	0.841 48	0.261 99	0.241 61	1.084 35	2N155489638FFL9700P0655L0M1.img
11	2.283 10	0.902 30	0.224 16	0.387 54	0.578 42	2N155489638FFL9700P0655L0M1.img
12	0.383 90	0.816 03	0.180 35	0.166 44	1.083 57	2N155489725FFL9700P0655L0M1.img
13	0.296 18	0.883 53	0.282 13	0.532 13	0.530 19	2N155489725FFL9700P0655L0M1.img
14	0.175 30	0.599 98	0.120 21	0.204 48	0.587 88	2N155669057FFL9800P0667L0M1.img
15	0.602 00	0.857 57	0.324 71	0.579 24	0.560 58	2N155669057FFL9800P0667L0M1.img
16	0.518 45	0.772 88	0.234 78	0.438 61	0.535 28	2N157533335FFLA269P0755L0M1.img

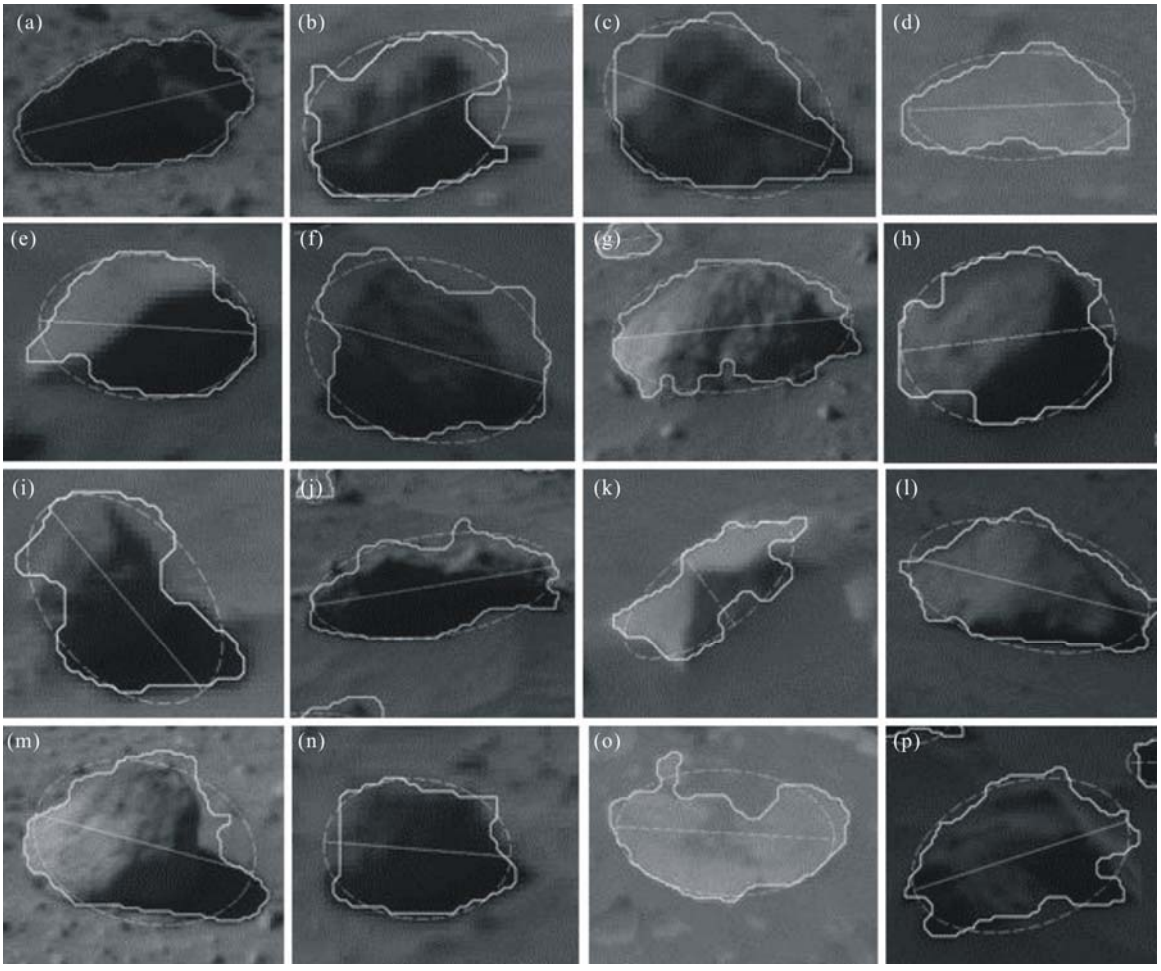

Figure 6. Extracted rocks and fitted ellipses (dashed lines).

engineering tasks.

It should be noted that in challenging areas with large slopes or where rocks are stuck together, the method might not be able to generate satisfactory results. This rock extraction method will be further enhanced to improve performance in these challenging areas.

REFERENCES CITED

Alexander, D. A., Deen, R. G., Andres, P. M., et al., 2006. Processing of Mars Exploration Rover Imagery for Science and Operations Planning. *Journal of Geophysical Research—Planets*, 111(E2): E02S02, doi:10.1029/2005 JE002462

Anderson, R. C., Castano, R., Stough, T., et al., 2001. Using Scaled Visual Texture for Autonomous Rock Clustering. Lunar and Planetary Science XXXII, Houston, http://www. lpi.usra.edu/meetings/lpsc2001/pdf/2103.pdf

Castano, R., Anderson, R. C., Fox, J., et al., 2002. Automating Shape Analysis of Rocks on Mars. Lunar and Planetary Science XXXIII, Houston, http://www.lpi.usra.edu/meetings/lpsc2002/pdf/2000.pdf

Castano, R., Judd, M., Estlin, T., et al., 2005. Current Results from a Rover Science Data Analysis System. In: IEEE Aerospace Conference, Montana, http://trs-new.jpl. nasa.gov/dspace/bitstream/2014/39275/1/05-0185.pdf

Castano, R., Estlin, T., Anderson, R. C., et al., 2007. Onboard Autonomous Rover Science. In: Proceedings of IEEE Aerospace Conference, http://marstech.jpl.nasa.gov/ publications/CastanoIEEE-Aero2007.pdf

Cheng, Y. Z., 1995. Mean Shift, Mode Seeking, and Clustering. *IEEE Transactions on Pattern Analysis and Machine Intelligence*, 17(8): 790–799

Comaniciu, D., Ramesh, V., Meer, P., 2000. Real-Time Tracking of Non-Rigid Objects Using Mean Shift. In: Conference on Computer Vision and Pattern Recognition, Hilton Head, SC. 142–149

Comaniciu, D., Ramesh, V., Meer, P., 2001. The Variable Bandwidth Mean Shift and Data-Driven Scale Selection. *Computer Vision*, 1: 438–445

Comaniciu, D., Meer, P., 2002. Mean Shift: A Robust Approach toward Feature Space Analysis. *Pattern Analysis and Machine Intelligence*, 24(5): 603–619

Comaniciu, 2009. Code for the Edge Detection and Image Segmentation System. http://coewww.rutgers.edu/riul/research/code/EDISON/doc/help.html [Accessed September 19, 2012]

Di, K., Xu, F., Wang, J., et al., 2008. Photogrammetric Processing of Rover Imagery of the 2003 Mars Exploration Rover Mission. *ISPRS Journal of Photogrammetry and Remote Sensing*, 63(2): 181–201, doi:10.1016/j. isprsjprs.2007.07. 007

Fitzgibbon, A., Pilu, M., Fisher, R. B., 1999. Direct Least-Square Fitting of Ellipses. *Pattern Analysis and Machine Intelligence*, 21(5): 476–480

Fox, J., Castano, R., Anderson, R. C., 2002. Onboard Autonomous Rock Shape Analysis for Mars Rovers. In: Proceedings of IEEE Aerospace Conference, Montana. 2036–2052

Fukanaga, K., Hostetler, L. D., 1975. The Estimation of the Gradient of a Density Function, with Applications in Pattern Recognition. *IEEE Transactions on Information Theory*, 21(1): 32–40

Golombek, M. P., Huertas, A., Marlow, J., et al., 2008, Size-Frequency Distributions of Rocks on the Northern Plains of Mars with Special Reference to Phoenix Landing Surfaces. *Journal of Geophysical Research—Planets*, 13(E00A09): 32, doi:10.1029/2007 JE003065

Gor, V., Castano, R., Manduchi, R., et al., 2001. Autonomous Rock Detection for Mars Terrain. In: Space 2001, American Institute of Aeronautics and Astronautics, Albuquerque, NM, USA

Gulick, V. C., Morris, R. L., Ruzon, M. A., et al., 2001. Autonomous Image Analyses during the 1999 Marsokhod Rover Field Test. *Journal of Geophysical Research*, 106(E4): 7745–7763, doi:10.1029/1999JE001182

Hong, Y., Yi, J., Zhao, D., 2007. Improved Mean Shift Segmentation Approach for Natural Images. *Applied Mathematics and Computation*, 185(2): 940–952

Li, R., Squyres, S. W., Arvidson, R. E., et al., 2005. Initial Results of Rover Localization and Topographic Mapping for the 2003 Mars Exploration Rover Mission. *Photogrammetric Engineering & Remote Sensing*, 71(10): 1129–1142

Li, R., Di, K., Howard, A. B., et al., 2007. Rock Modeling and Matching for Autonomous Long-Range Mars Rover Localization. *Journal of Field Robotics*, 24(3): 187–203, doi:10.1002/rob.20182

Manduchi, R., Pollara, F., Dolinar, S., et al., 2000. Onboard Science Processing and Buffer Management for Intelligent Deep Space Communications. In: Proceedings of IEEE Aerospace Conference Big Sky, Montana, USA, http://trs-new.jpl.nasa.gov/dspace/bitstream/2014/18495/1/99-1983. pdf

Ozertem, U., Erdogmus, D., Jenssen, R., 2008. Mean Shift Spectral Clustering. *Pattern Recognition*, 41(6): 1924–1938

Peng, N. S., Yang, J., Liu, Z., et al., 2005. Automatic Selection of Kernel-Bandwidth for Mean-Shift Object Tracking. *Journal of Software*, 16(9): 1542–1550, doi:10.1360/jos161542 (in Chinese with English Abstract)

Song, Y. H., Shan, J., 2006. A Framework for Automated Rock Segmentation of the Mars Exploration Rover Imagery. In: Proceedings of ASPRS 2006 Annual Conference, Reno, Nevada, USA

Song, Y. H., Shan, J., 2008. Automated Rock Segmentation for Mars Exploration Rover Imagery. In: Lunar and Planetary Science Conference XXXIX, Houston, USA

Thompson, D. R., Niekum, S., Smith, T., et al., 2005a. Automatic Detection and Classification of Features of Geologic Interest. In: Proceedings of IEEE Aerospace Conference, Montana, USA

Thompson, D. R., Smith, T., Wettergreen, D., 2005b. Data Mining during Rover Traverse: From Images to Geologic Signatures. In: Proceedings of 8th International Symposium on Artificial Intelligence, Robotics and Automation in Space, USA, http://www.ri.cmu.edu/ pub_files/pub4/thompon_david_r_2005_3/thompson_david_r_2005_3.pdf

Thompson, D. R., Castano, R., 2007. Performance Comparison of Rock Detection Algorithms for Autonomous Planetary Geology. Aerospace, IEEE, USA, IEEEAC Paper No. 1251, http://www.davidraythompson.com/publica-tions/2007_IEEEAerospace_Thompson.pdf

Wagstaff, K. L., Castano, R., Dolinar, S., et al., 2004. Science-Based Region-of-Interest Image Compression. In: Proceedings of 35th Lunar and Planetary Science Conference, League City, Texas, USA, http://www.litech.org/~wkiri/Papers/wagstaff-lpsc04.pdf

Wen, Z. Q., Cai, Z. X., 2007. Convergence Analysis of Mean Shift Algorithm. *Journal of Software*, 18(2): 205–212, doi:10.1360/jos180205 (in Chinese with English Abstract)

Wu, K. L., Yang, M. S., 2007. Mean Shift-Based Clustering. *Pattern Recognition*, 40(11): 3035–3052

Xu, C. Y., Prince, J. L., 1997. Gradient Vector Flow: A New External Force for Snakes. In: Proceedings of IEEE Computer Society Conference on Computer Vision and Pattern Recognition. 66–71